PHYSICAL REVIEW B **90**, 155204 (2014)

Optoelectronic properties of Ta_3N_5: A joint theoretical and experimental study

Juliana M. Morbec,[1] Ieva Narkeviciute,[2] Thomas F. Jaramillo,[2] and Giulia Galli[1]
[1] *Institute for Molecular Engineering, University of Chicago, Chicago, Illinois 60637, USA*
[2] *Department of Chemical Engineering, Stanford University, Stanford, California 94305, USA*

(Received 5 August 2014; revised manuscript received 5 October 2014; published 27 October 2014)

A joint theoretical and experimental study of the optoelectronic properties of Ta_3N_5 was conducted by means of *ab initio* calculations and ellipsometry measurements. Previous experimental work on Ta_3N_5 has not been conclusive regarding the direct or indirect nature of light absorption. Our work found excellent agreement between the optical spectrum computed using the Bethe-Salpeter equation and the measured one, with two prominent features occurring at 2.1 and 2.5 eV assigned to direct transitions between N and Ta states. The computed optical gap, obtained from the G_0W_0 direct photoemission gap, including spin-orbit coupling, electron-phonon renormalization of the conduction band, and exciton binding energy, was found to be in excellent agreement with measurements. Our results also showed that Ta_3N_5 is a highly anisotropic material with heavy holes in several directions, suggesting low hole mobilities, consistent with low measured photocurrents in the Ta_3N_5 literature.

DOI: 10.1103/PhysRevB.90.155204 PACS number(s): 71.20.−b, 71.35.Cc, 78.20.−e

I. INTRODUCTION

Since the pioneering work of Fujishima and Honda [1] in 1972 reporting the photoelectrochemical (PEC) decomposition of water in a Pt-TiO_2 cell, various semiconductors—most of them oxides—have been investigated as potential materials for application in photoelectrochemical cells [2]. Among several attractive candidates, tantalum nitride (Ta_3N_5) appears promising due to its suitable band gap for visible light absorption and favorable band-edge positions for water splitting. In particular, recent electrochemical and spectroscopic measurements have shown that the conduction and valence bands of Ta_3N_5 straddle the H^+/H_2O and O_2/H_2O redox potentials [3], possibly allowing Ta_3N_5 to perform unassisted water splitting. In addition, considering complete absorption and 100% utilization of photons higher in energy than the band gap, this material could exhibit a photocurrent of 12.5 mA/cm^2 [4]. However, photoelectrochemical measurements of several Ta_3N_5 samples in different conditions have reported photocurrents less than 7 mA/cm^2, even with an applied bias and in the presence of electrocatalysts [5,6].

Aiming to fully characterize the optoelectronic properties of Ta_3N_5 and to understand possible reasons for the limited photocurrent, we have performed a joint experimental and *ab initio* theoretical study of Ta_3N_5. *Ab initio* calculations were carried out using density functional theory [7] (with local, semilocal, and hybrid exchange-correlation functionals) and many-body perturbation theory (at the G_0W_0 level) [8,9], and the optical absorption spectra were computed by solving the Bethe-Salpeter equation (BSE) [8,10]. We also used *ab initio* calculations to compute the effective masses of holes and electrons, and gain insight into the carrier transport properties of Ta_3N_5. In addition, we experimentally measured the dielectric function with ellipsometry.

In this work we present a detailed analysis of the optoelectronic properties of Ta_3N_5, showing that the material is highly anisotropic, with heavy holes in several directions, pointing to low mobilities. The excellent agreement found between measured and computed optical spectra allowed us to provide an interpretation of the main absorption onsets, found to be direct transitions between N and Ta states. We also discuss the differences between direct and indirect gaps and between photoemission and optical gaps.

The rest of the paper is organized as follows: in Sec. II we describe the details of our *ab initio* calculations and ellipsometry experiments; in Sec. III we present our results for the structural properties, electronic gap and effective masses, optical band gap, optical spectra, and spectroscopic ellipsometry; and in Sec. IV we provide our conclusions.

II. COMPUTATIONAL AND EXPERIMENTAL TECHNIQUES

A. *Ab initio* calculations

The ground state structural and electronic properties of Ta_3N_5 were calculated using density functional theory (DFT). We used exchange-correlation functionals within the local density approximation (LDA) [11] and the Perdew-Burke-Ernzerhof generalized gradient approximation (GGA-PBE) [12], as well as hybrid functionals, namely PBE0 [13] and the sc-hybrid functional proposed in Ref. [14] that employs a mixing parameter derived self-consistently from the macroscopic dielectric function.

In most of the DFT calculations we employed the QUANTUM ESPRESSO (QE) [15] package, plane-wave basis sets with energy cutoff of 160 Ry, and norm-conserving Hartwigsen-Goedecker-Hutter (HGH) [16] pseudopotentials (Ta $5s^2 5p^6 5d^3 6s^2$ and N $2s^2 2p^3$ states were treated as valence states). We also carried out calculations using localized basis sets, in particular the linear combination of atomic orbitals method as implemented in CRYSTAL09 [17]. In this case, we employed an all-electron Gaussian-type 7-311G* basis set [18] for the N atoms; for the Ta atoms we adopted the Hay-Wadt small-core effective core pseudopotential [19] and we variationally optimized the exponents of the valence states, first for the isolated ion Ta^{+5} and then for Ta_3N_5. We used 242 and 301 k points in the QE and CRYSTAL09 calculations, respectively. (We assessed the convergence of the k-point mesh in QE calculations by comparing results for the structural properties and electronic gaps at the PBE level, obtained with 242 and 476 k points, which were identical.)

1098-0121/2014/90(15)/155204(10)

We calculated the quasiparticle energies using many-body perturbation theory (MBPT) at the G_0W_0 level. The G_0W_0 calculations were performed starting from DFT/PBE orbitals using the YAMBO code [20]. The calculated G_0W_0 band gap as well as valence band maximum (VBM) and conduction band minimum (CBM) were converged within 0.05 eV with respect to the numerical parameters, namely number of bands, size of the dielectric matrix and screened Coulomb potential, k-point mesh, and energy cutoff for the ground state wave functions. In the G_0W_0 scheme the independent-particle Green's function G_0 and the screened Coulomb interaction W_0 are evaluated non-self-consistently using Kohn-Sham eigenvalues and single particle orbitals. In this work we did not investigate the effect of self-consistency; based on the G_0W_0 and self-consistent results reported in Ref. [21] for oxides and some nitrides (starting from Kohn-Sham orbitals obtained with gradient corrected functionals), we estimate the error introduced by the lack of self-consistency to be smaller than 10% for the G_0W_0 value of the electronic gap of Ta_3N_5. The optical absorption spectra were obtained by solving the Bethe-Salpeter equation (BSE) [8–10], starting from our G_0W_0 results and employing the double-grid method for k-point sampling [22].

B. Ta_3N_5 sample preparation

In our sample preparation, 29 nm of Ta metal were deposited onto Si(100) wafers by electron beam evaporation (Innotec ES26C). These films were oxidized at 700 °C in a gaseous stream of 20 sccm O_2 and 80 sccm Ar for 1 h to form Ta_2O_5 and subsequently nitrided at 850 °C in 50 sccm of gaseous NH_3 for 8 h in a tube furnace to make Ta_3N_5 (Mellen Company SC12.5R, three zones). This procedure yielded a film of 60 nm thickness as measured by cross-sectional scanning electron microscopy, SEM (FEI Magellan 400 XHR, 5 kV). X-ray diffraction (XRD) (PANanalytical X'Pert Pro Materials Research Diffractometer) was performed with Cu $K\alpha$ radiation in specular reflection mode to ensure the desired Ta_3N_5 phase was formed when compared to a powder diffraction reference sample (PDF reference code 01-079-1533).

C. Spectroscopic ellipsometry

Spectroscopic ellipsometry is a versatile optical tool that measures the polarization of reflected or transmitted light, and it allows for the determination of film thickness and optical constants of materials over a wide range of photon energies. It is a remarkably accurate technique but a drawback is its indirect nature, since the data has to be fit with optical models to determine the desired information and gain physical insight [23].

The data measured by spectroscopic ellipsometry are Ψ and Δ, which correspond to changes in the amplitude ratio and phase of s- and p-polarized light, respectively. Ψ and Δ are related by the complex reflection ratio ρ, i.e., the ratio of the Fresnel reflection coefficients for s- and p-polarized light:

$$\rho = \frac{r_p}{r_s} = \tan\Psi \exp(i\Delta) = \frac{\frac{E_{\rm rp}}{E_{\rm ip}}}{\frac{E_{\rm rs}}{E_{\rm is}}}, \qquad (1)$$

where $E_{\rm rp}$ and $E_{\rm rs}$ are the reflected electric fields for s- and p-polarized light, respectively, and $E_{\rm ip}$ and $E_{\rm is}$ are the incident electric fields [23].

Ellipsometry data is typically modeled as a sum of oscillators of given strength, to determine the optical constants and/or thickness of the material being analyzed. The optical constants, namely the refractive index n and the extinction coefficient k, provide insight on the amount of atomic and electric polarization occurring in the material, and they are related to the dielectric constant $\varepsilon = \varepsilon_1 + i\varepsilon_2$ [23], where $\varepsilon = N^2$ and $N = n + ik$ is the complex refractive index. Hence, $\varepsilon_1 = n^2 - k^2$ and $\varepsilon_2 = 2nk$.

Reflectance-mode ellipsometry was performed with a J. A. Woollam M2000 ellipsometer centered around the Brewster angle for the silicon substrate (70°) at three 5° intervals over a photon range of 0.7 to 6 eV. Optical modeling was conducted with WVase32 software by J. A. Woollam [24]. The data model took into account the presence of three layers, i.e., a semi-infinite Si substrate, the native SiO_2 layer, and Ta_3N_5, where we used Drude, Tauc-Lorentz, and effective medium approximation (EMA) models. The native SiO_2 layer thickness was measured using ellipsometry prior to Ta metal deposition as 16.36 Å and assumed to be unchanged after the oxidation and nitridation of Ta metal for the purposes of parametrization.

III. RESULTS AND DISCUSSION

A. Structural properties

The Ta_3N_5 crystal has an orthorhombic structure with space group $Cmcm$. The conventional unit cell consists of 32 atoms, where each Ta atom is bonded to six N atoms, while N atoms have three or four Ta atoms (see Fig. 1). In order to check the validity of our computational scheme, we first optimized the geometry of Ta_3N_5 using DFT calculations with both LDA and PBE exchange-correlation functionals. As shown in Table I our optimized lattice parameters are in good agreement with the experimental results [25] as well as with previous theoretical works [26–29]. Our calculated bond

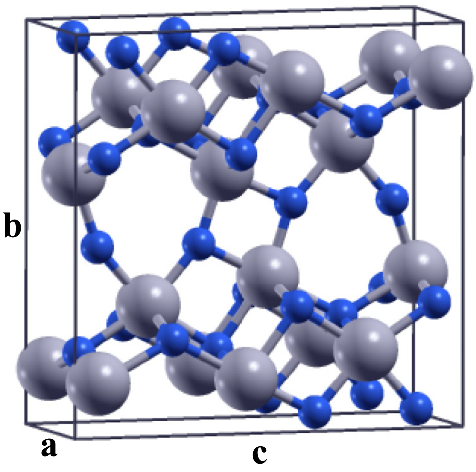

FIG. 1. (Color online) The crystal structure of Ta_3N_5. The solid has an orthorhombic structure with space group $Cmcm$. Ta and N atoms are shown as gray and blue spheres, respectively. Ta has six neighbors and N has three or four neighbors.

TABLE I. Calculated lattice parameters (see Fig. 1) and volume of Ta$_3$N$_5$, obtained using DFT. The functional and code (within parentheses) used in the calculation are given in column 1.

Functional	a (Å)	b (Å)	c (Å)	Volume (Å^3)
This work				
PBE (QE)	3.87	10.22	10.26	406.41
PBE (CRYSTAL)	3.90	10.33	10.32	415.80
LDA (QE)	3.85	10.14	10.16	396.40
Previous work				
revPBE[a]	3.99	10.69	10.69	455.96
PBE[b]	3.87	10.24	10.26	406.59
PBE[c]	3.91	10.32	10.35	417.63
GGA + U[d]	4.00	10.43	10.48	437.23
HSE[d]	3.87	10.25	10.27	407.38
Experiment[e]	3.89	10.21	10.26	407.26

[a] Reference [26]: localized basis set, Troullier-Martins norm conserving pseudopotentials, SIESTA code.

[b] Reference [27]: plane-wave basis set with kinetic energy cutoff of 500 eV, 10 × 8 × 4 k-point mesh, VASP code.

[c] Reference [28]: plane-wave basis set with kinetic energy cutoff of 500 eV, Ta $5p^6 5d^4 6s^1$ orbitals in the valence state, VASP code.

[d] Reference [29]: plane-wave basis set with energy cutoff of 500 eV for GGA + U and 400 eV for HSE calculation, Ta $5p^6 5d^4 6s^1$ orbitals in the valence state, VASP code.

[e] Reference [25].

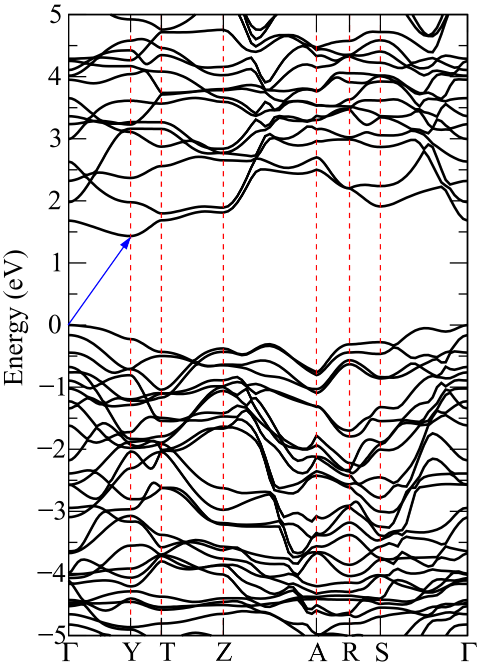

FIG. 2. (Color online) Band structure of Ta$_3$N$_5$, obtained using DFT/PBE at the experimental geometry. The blue arrow indicates the indirect band gap Γ-Y. Note the small difference with the direct gap at Γ.

lengths and angles (not shown) are within ±0.60% (using PBE) and ±1.30% (using LDA) of the experimental values [25], which indicates that both LDA and PBE satisfactorily describe the structural properties of Ta$_3$N$_5$.

B. Electronic gap and effective masses

Recent UV-vis measurements of Ta$_3$N$_5$ powders [3] and thin films [30,31] have shown that the absorption edge occurs near 600 nm, indicating that Ta$_3$N$_5$ has an optical gap of about 2.1 eV. We investigated the electronic structure of Ta$_3$N$_5$ using both DFT (with LDA, GGA, and hybrid funcionals) and MBPT (within the G_0W_0 approximation). The DFT/PBE and DFT/LDA calculations were performed at the experimental and optimized geometries, while hybrid functionals and G_0W_0 calculations were carried out only at the experimental geometry, which is very close to the theoretical one at the PBE level (see Table I). We found that Ta$_3$N$_5$ is an indirect band-gap semiconductor with the VBM located at the Γ point and the CBM located at Y point (see Fig. 2). The density of states displayed in Fig. 3 shows that the top of the valence band is mainly composed of N $2p$ orbitals, while the bottom of the conduction band is mainly composed of Ta $5d$ orbitals. This is in agreement with previous work [29,33,34] and indicates that the transitions near the absorption edge occur between N $2p$ and Ta $5d$ orbitals.

Table II shows our calculated direct and indirect electronic band gaps, as well as results reported previously [27,29,33–35]. As expected, the DFT/PBE and DFT/LDA band gaps are underestimated when compared to the experimental result (2.1 eV); the PBE0 hybrid functional, on the other hand, strongly overestimates the band gaps. As discussed in Ref. [14] this large overestimate may partly stem from the mixing parameter α used in PBE0 calculations, and the results can be improved by setting α equal to the inverse of the high-frequency dielectric constant ε_∞. We used the self-consistent hybrid mixing scheme (sc-hybrid) proposed in Ref. [14] with $\alpha = 1/\text{sc-}\varepsilon_\infty$, where sc-$\varepsilon_\infty$ was computed self-consistently (sc) using the coupled perturbed Kohn-Sham (CPKS) [37] method as implemented in CRYSTAL09. We obtained a self-consistent value for the dielectric constant (sc-ε_∞) equal to

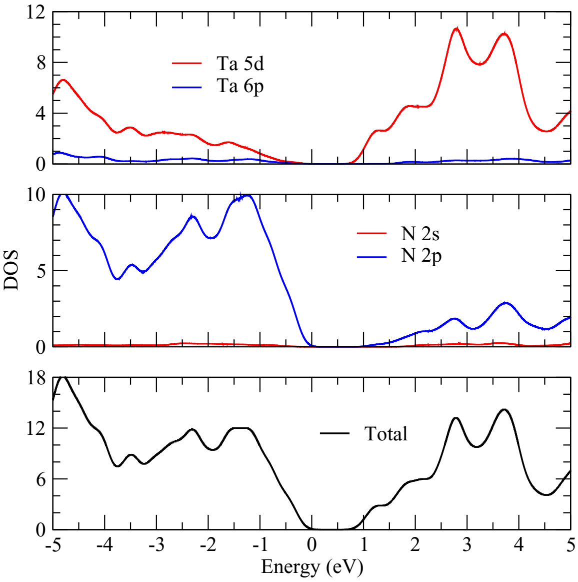

FIG. 3. (Color online) Partial [upper (Ta) and middle (N) panels] and total (lower) density of states (DOS) of Ta$_3$N$_5$, obtained using DFT/PBE at the experimental geometry [32].

TABLE II. Direct (E_g^D) and indirect (E_g^I) electronic band gaps of Ta_3N_5 calculated using DFT (with various exchange-correlation functionals specified in column 1) and many body perturbation theory within the G_0W_0 approximation. We considered both experimental and optimized geometries. Direct band gaps are listed at Γ and Y points (see Fig. 2). Unless otherwise specified, our DFT results were obtained using the QUANTUM ESPRESSO code.

Functional	E_g^I (eV) Γ-Y	E_g^D (eV) Γ point	E_g^D (eV) Y point
Experimental geometry			
PBE	1.43, 1.26[a]	1.68, 1.49[a]	1.66, 1.54[a]
LDA	1.27	1.52	1.50
PBE0	2.79[a]	3.05[a]	3.15[a]
sc-hybrid ($\alpha = 1/\text{sc-}\varepsilon_\infty$)[b]	1.88[a]	2.12[a]	2.19[a]
G_0W_0	1.93	2.23	2.22
Optimized geometry			
PBE	1.43, 1.29[a]	1.66, 1.50[a]	1.66, 1.55[a]
LDA	1.22	1.46	1.51
Previous work			
PBE	1.27[c], 1.2[d] 1.2[e], 1.25[f]	1.4[d]	
PW91	1.1[g]	1.4[g]	
EVGGA	1.5[e]		
LDA	1.1[e]		
GGA + U	2.1[c]	2.3[c]	
mBJ[h]	2.1[e]		
PBE0	2.91[f]		
HSE	2.20[c], 2.21[f] 1.81[i]		
Δ-sol	2.37[i]		

[a] Obtained using the CRYSTAL09 code.

[b] Functional defined as in Ref. [14].

[c] Reference [29]: plane-wave basis set with energy cutoff of 500 eV for PBE and GGA + U calculations and 400 eV for HSE calculation, Ta $5p^6 5d^4 6s^1$ orbitals in the valence state, VASP code, optimized geometry.

[d] Reference [33]: full-potential linear augmented-plane-wave (FLAPW) method, WIEN97 code, experimental geometry.

[e] Reference [34]: full-potential linear augmented-plane-wave (FLAPW) method, WIEN2k code, experimental geometry.

[f] Reference [35]: plane-wave basis set with energy cutoff of 450 eV, 4 × 2 × 2 k-point mesh, VASP code, PBE optimized geometry.

[g] Reference [33]: plane-wave basis set with energy cutoff of 36 Ry, Vanderbilt ultrasoft pseudopotentials, 6 × 6 × 6 k-point mesh, VASP code, experimental geometry.

[h] Modified Becke-Johnson potential [36].

[i] Reference [27]: plane-wave basis set, VASP code, PBE optimized geometry; energy cutoff of 520 eV and 7 × 7 × 3 k-point mesh for the HSE calculation, and 500 eV and 10 × 8 × 4 k-point mesh for the Δ-sol calculation.

9.17 and, as shown in Table II, we found an indirect band gap of 1.88 eV and direct band gaps of 2.12 (Γ point) and 2.19 eV (Y point), which are in good agreement with experiment.

However, the sc-hybrid results were obtained with localized basis set and they may be 0.1–0.2 eV lower than the corresponding fully converged results. Indeed, the DFT/PBE gaps obtained using the CRYSTAL09 code differ from those obtained using the QE package by 0.11–0.19 eV, due to the difference in basis sets and pseudopotentials employed in the two calculations. Since the plane-wave cutoff was fully converged and the pseudopotentials used in QE at the PBE level are consistent with the treatment of the interaction between the valence electrons (the Hay-Wadt pseudopotential used in CRYSTAL09 is derived at the Hartree-Fock level of theory), we consider the plane-wave results as the best numerical results for Ta_3N_5 at the DFT/PBE level of theory. Hence approximately all PBE gaps obtained using CRYSTAL09 for this system are most likely underestimated by 0.1–0.2 eV. Assuming the same underestimate holds at the hybrid functional level, our extrapolated PBE0 gap is in agreement with that of Ref. [35].

We note that the inclusion of Ta $5s$ and $5p$ semicore states in the valence partition is important to obtain accurate band gaps and structural parameters. Tests were conducted at the PBE and LDA levels: see Supplemental Material [38]. For example, without semicore states, i.e., with only Ta $5d^3 6s^2$ states treated as valence states, using the PBE functional and the experimental geometry, we found indirect and direct (at the Γ point) band gaps of 1.18 and 1.43 eV, respectively, which are 0.25 eV smaller than those obtained with Ta $5s$ and $5p$ semicore states in the valence [38]. These results may explain some of the discrepancies between ours and previous numbers reported in the literature.

Finally we checked the effect of the spin-orbit interaction on the band structure of Ta_3N_5 at the DFT/PBE level and the experimental geometry by using full relativistic pseudopotentials. We obtained small decreases of 0.03 eV in both direct and indirect band gaps obtained without spin-orbit coupling.

Quasiparticle (QP) gaps were computed at the G_0W_0 level using DFT/PBE wave functions at the experimental geometry, and they are reported in Table III (note that we used 3 × 3 × 3 k-point mesh and 80 Ry for the calculation shown in Table III and 12 × 6 × 6 k-point mesh and 160 Ry cutoff energy to obtain the DFT/PBE results listed in Table II). We found that the highest occupied states at the Γ and Y points are shifted to lower energy by 0.04 and 0.09 eV, respectively, while the lowest unoccupied states are shifted upward by 0.54 and 0.49 eV. This results in a QP indirect band gap (Γ-Y) of 1.93 eV and direct band gaps of 2.23 (Γ point) and 2.22 (Y point) eV, in excellent agreement with the converged results of sc-hybrids. Note that the G_0W_0 correction to the band gap of Ta_3N_5 comes mainly from the shift of the conduction band, and this shift is not rigid. We found that the difference between our calculated QP indirect band gap and the lowest QP direct

TABLE III. Energy (eV) of the highest occupied and lowest unoccupied states, computed at the DFT/PBE and G_0W_0 levels of theory, at different k points (see Fig. 2). The highest occupied state at the Γ point computed at the DFT/PBE level of theory is set to zero energy.

	Γ	T	Y	A	R
DFT/PBE					
Highest occupied	0.00	−0.44	−0.24	−0.77	−0.32
Lowest unoccupied	1.65	1.66	1.40	2.48	2.17
G_0W_0					
Highest occupied	−0.04	−0.55	−0.33	−0.99	−0.45
Lowest unoccupied	2.19	2.18	1.89	3.03	2.68

TABLE IV. Effective masses (m^*) of holes and electrons obtained from quadratic fits of the band structure of Ta_3N_5 computed at the DFT/PBE level of theory at the experimental geometry. m_0 is the electron mass.

	m^*/m_0				
Holes	0.66 (ΓX)	0.27 (ΓZ)	3.56 (ΓY)	0.32 ($Y X_1$)	0.72 ($Y T$)
Electrons	0.23 (ΓX)	1.70 (ΓZ)	2.70 ($Y \Gamma$)	0.21 ($Y X_1$)	0.85 ($Y T$)

band gap is 0.29 eV, similar to those obtained at the DFT/PBE and DFT/LDA levels of theory (between 0.23 and 0.28 eV).

To gain insight into the carrier transport properties of Ta_3N_5 we computed the effective masses of holes (m_h^*) and electrons (m_e^*) from quadratic fits of the bands (we considered the band structure obtained using DFT/PBE at the experimental geometry). Our results, presented in Table IV, show that both electrons and holes have large effective masses along some directions; for example, we found $m_e^* = 2.70 m_0$ along Y-Γ and $m_h^* = 3.56 m_0$ along Γ-Y direction. This suggests that Ta_3N_5 may have low carrier mobilities and hence poor bulk charge transport properties, which can be one of the causes of the low photocurrents (less than 60% of the theoretical limit) reported for this material.

Recently, Pinaud *et al.* [39] investigated the photoactivity of Ta_3N_5/Ta photoanodes as a function of the film thickness and morphology, finding that both electron and hole mobilities can affect the performance of Ta_3N_5 photoanodes. The photocurrent appeared to scale primarily with surface area (large surface areas improve hole collection at the solid/liquid interface) rather than with thickness (related to the electron mean free path), indicating that the hole transport plays a major role. The results of Table IV are consistent with this finding: The effective masses of holes are larger than those for electrons in most directions, indicating that holes have lower mobility than electrons and are the limiting factor in the generated photocurrent.

TABLE V. High-frequency (ε_∞) and static (ε_0) dielectric constants of Ta_3N_5 obtained using several levels of theory. All calculations were carried out at the experimental geometry. In the sc-hybrid calculation, the mixing parameter α was self-consistently determined from the high-frequency dielectric constant ($\alpha = 1/\varepsilon_\infty$), as proposed in Ref. [14].

	ε_∞ (PBE)[a]	ε_∞ (PBE)[b]	ε_∞ (PBE0)[b]	ε_∞ (sc-hybrid)[b]	ε_0 (PBE)[a]
xx	10.71	10.74	8.00	9.25	35.80
yy	10.52	10.47	8.37	9.39	43.51
zz	9.70	9.99	7.86	8.86	86.46
Average[c]	10.31	10.40	8.08	9.17	55.26

[a] Obtained using plane-wave basis set, density functional perturbation theory and the QE code.

[b] Obtained using localized basis set and the CPKS method as implemented in CRYSTAL09.

[c] $\varepsilon^{\mathrm{average}} = (\varepsilon^{xx} + \varepsilon^{yy} + \varepsilon^{zz})/3$.

C. Optical band gap

To predict the optical band gap from our calculated QP band gap we computed the exciton binding energy and estimated the effect of electron-phonon interaction on the computed energy levels. To obtain the latter we followed the procedure adopted in Ref. [40]: Considering the Fröhlich Hamiltonian model [41] and the Rayleigh-Schrödinger perturbation theory [42], the renormalization of the conduction band at the Γ point is given by

$$\Delta E = -\hbar\omega_{\mathrm{LO}}[\alpha + 0.0159\alpha^2 + 0.000806\alpha^3 + O(\alpha^4)], \tag{2}$$

where ω_{LO} is the longitudinal optical phonon frequency and

$$\alpha = \frac{e^2}{\hbar}\left(\frac{m^*}{2\hbar\omega_{\mathrm{LO}}}\right)^{1/2}\left(\frac{1}{\varepsilon_\infty} - \frac{1}{\varepsilon_0}\right) \tag{3}$$

is the coupling constant. Here m^* is the conduction band effective mass and ε_∞ and ε_0 are the high-frequency (electronic contribution) and static (ionic and electronic contributions) dielectric constants, respectively. ε_0 was obtained using

$$\varepsilon_0^{\alpha\beta} = \varepsilon_\infty^{\alpha\beta} + \frac{4\pi}{\Omega}\sum_m \frac{\left[\sum_{k\alpha'} Z^*_{k\alpha\alpha'} U^*_{m\mathbf{q}=0}(k\alpha')\right]\left[\sum_{k'\beta'} Z^*_{k'\beta\beta'} U^*_{m\mathbf{q}=0}(k'\beta')\right]}{\omega_m^2}, \tag{4}$$

where Z^* are the Bohr effective charges, $U^*_{m\mathbf{q}=0}$ are the eigenmodes of the dynamical matrix at $\mathbf{q} = 0$, and ω_m are the vibrational frequencies.

We calculated ω_{LO}, ε_∞, and ε_0 using density functional perturbation theory [43] at the DFT/PBE level of theory and at the experimental geometry, and employing the QE code. By considering the highest optical phonon frequency we found $\hbar\omega_{\mathrm{LO}} = 0.108$ eV. The diagonal components of ε_∞ and ε_0 are listed in Table V (columns 2 and 6, respectively). We also computed ε_∞ using the CPKS method as implemented in CRYSTAL09. In this case, we employed the PBE and PBE0 functionals as well as the sc-hybrid functional [14] with $\alpha = 1/\varepsilon_\infty$. The results of these calculations are listed in columns 3, 4, and 5 of Table V. We found an excellent agreement, at the PBE level, between the values obtained using plane-wave basis set and density functional perturbation theory (column 2) and those computed employing localized basis set and the CPKS method (column 3). We also note that our $\varepsilon_\infty^{\mathrm{average}} = 8.08$–$10.40$ agrees with previous theoretical results (7.20–10.80) [29,34] obtained using different levels of theory, namely LDA, PBE, GGA + U, EVGGA, and mBJ.

By taking the average values of $m^*_{e\Gamma}$ ($0.96 m_0$), $\varepsilon_\infty^{\mathrm{PBE}}$ (10.31), and $\varepsilon_0^{\mathrm{PBE}}$ (55.26), and using Eqs. (2) and (3), we found $\alpha = 0.87$ and $\Delta E = -0.09$ eV, which indicates a decrease of 0.09 eV in the band gap at the Γ point due to the electron-phonon interaction. If we consider the single values of $m^*_{e\Gamma}$, $\varepsilon_\infty^{\mathrm{PBE}}$, and $\varepsilon_0^{\mathrm{PBE}}$ in the x, y, and z directions, instead of the averages, we obtain values of ΔE ranging from -0.04 to -0.15 eV. We also found $\Delta E = -0.13$ and -0.11 eV when we used $\varepsilon_\infty^{\mathrm{average}}(\mathrm{PBE0}) = 8.08$ and $\varepsilon_\infty^{\mathrm{average}}(\text{sc-hybrid}) = 9.17$, respectively, in Eq. (2).

The exciton binding E_b can be calculated as the difference between the first excitation energy of the optical spectrum (see

Sec. III D) and the QP band gap. We found $E_b \approx 0.05$ eV, which is smaller than (but in reasonable agreement with) the values 0.07, 0.12, and 0.09 eV estimated from the hydrogenic model [44]

$$E_b = \frac{\mu}{m_0 \varepsilon^2} R_{\mathrm{H}} \tag{5}$$

using $\varepsilon = \varepsilon_\infty^{\text{average}} = 10.31$ (PBE), 8.08 (PBE0), and 9.17 (sc-hybrid), respectively. Here μ is the effective reduced mass ($1/\mu = 1/m_e^* + 1/m_h^*$), m_0 is the electron mass, and R_{H} is the Rydberg constant of the hydrogen atom (13.6 eV).

Therefore, from the QP gap at the G_0W_0 level of 2.23 eV (see Table II), considering the effects of spin-orbit (-0.03 eV), the electron-phonon interaction (-0.09 eV) and exciton binding (~ -0.05 eV), we obtain an optical direct band gap of 2.06 eV at the Γ point, in agreement with the experimental results. As discussed in Sec. II A, we expect the error introduced by the lack of self-consistency to be less than 10% [21] and most likely to amount to an increase of the computed G_0W_0 gap. Hence the value reported here (2.06 eV) might be an underestimate (of the order of 10%) of the self-consistent GW value, which could be as high as $\sim$2.28 eV, a value still in good agreement with experiments.

D. Optical spectra

In a recent work, Pinaud *et al.* [30] reported UV-vis absorption spectra collected on Ta_3N_5 thin films with different thicknesses. The spectra show two absorption edges at 600 nm (2.1 eV) and 500 nm (2.5 eV), respectively. In order to provide an interpretation of these edges, we computed the optical absorption spectrum at the BSE level of theory starting from G_0W_0 results. Since BSE calculations generally require a large number of k points, we employed the double-grid method proposed in Ref. [22] to speed up the convergence.

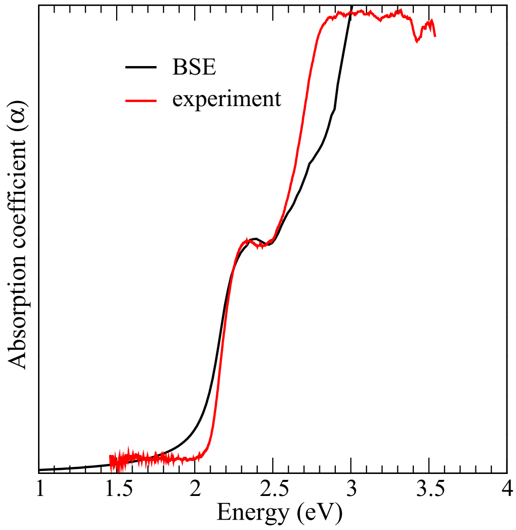

FIG. 4. (Color online) Absorption spectra of Ta_3N_5 computed using the Bethe-Salpeter equation (BSE), compared to the experimental result (from Ref. [30]) obtained with UV-vis spectroscopy. In our calculations we used a Lorentzian broadening of 0.1 eV.

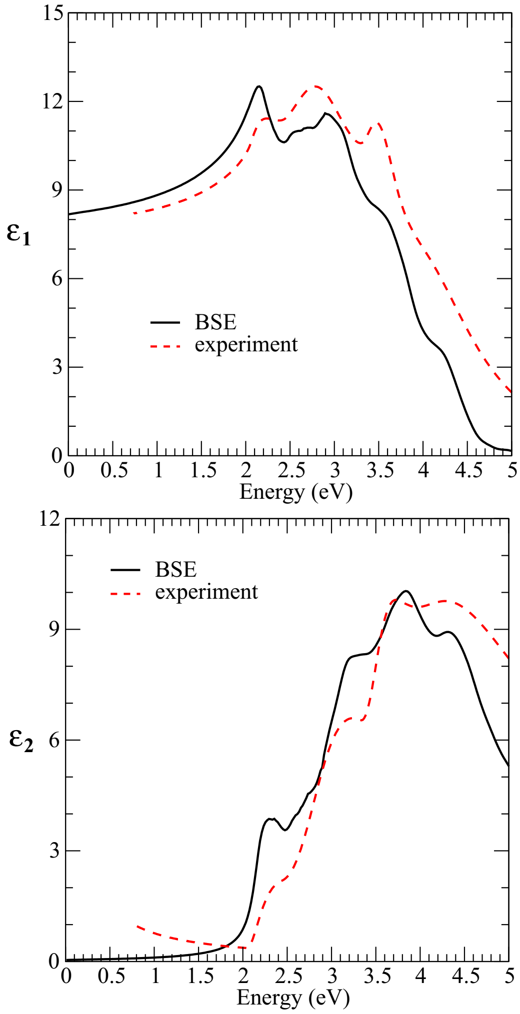

FIG. 5. (Color online) Dielectric functions ε of Ta_3N_5 computed using the Bethe-Salpeter equation (BSE), compared to the experimental results obtained using spectroscopic ellipsometry (see Sec. III E). In our calculations we used a Lorentzian broadening of 0.1 eV.

Figure 4 shows the absorption coefficient (α) of Ta_3N_5 computed at the BSE/G_0W_0 level of theory, compared with the experimental result obtained with UV-vis spectroscopy [30]. The absorption coefficient (α) was calculated from the dielectric function ($\varepsilon = \varepsilon_1 + i\varepsilon_2$):

$$\alpha(E) = \frac{\sqrt{2}E}{\hbar c}\sqrt{|\varepsilon(E)| - \varepsilon_1(E)}. \tag{6}$$

Our calculated dielectric functions ε_1 and ε_2 computed within BSE/G_0W_0 are shown in Fig. 5 and compare well with those obtained from ellipsometry measurements (see Sec. III E).

Both α and ε_2 computed within BSE/G_0W_0 exhibit two clear absorption features below 3 eV. The first one is an absorption edge at $\sim$2.0 eV, indicating that Ta_3N_5 has a direct band gap of $\sim$2.0 eV, while the second one has an onset at 2.5 eV. Since our BSE calculations do not include phonon-assisted transitions, these edges correspond to direct interband transitions. Our calculated density of states shown in Fig. 3 shows that both features correspond to direct transitions between N $2p$ and Ta $5d$ states.

From our BSE calculations of ε_1 we found $\varepsilon_1(0) \approx 8.17$, which is in satisfactory agreement with the value of 9.17

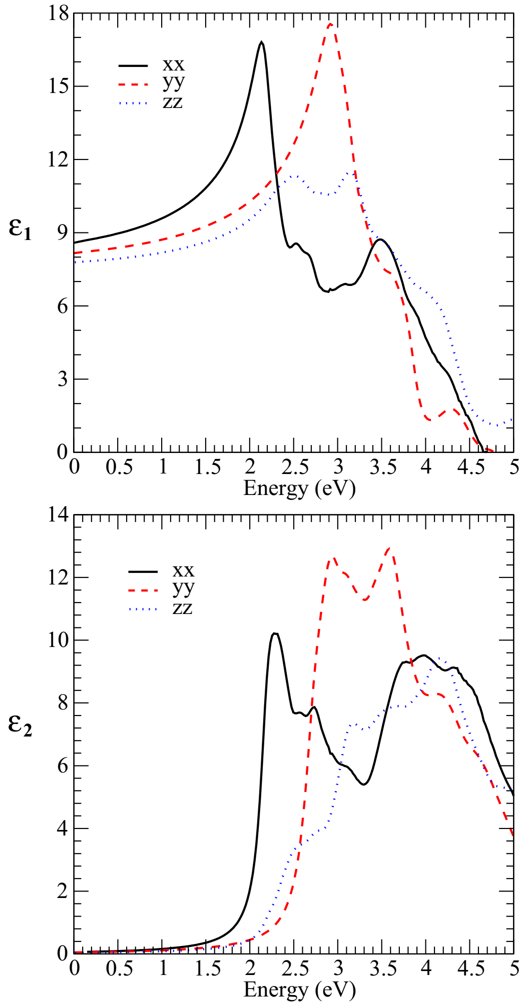

FIG. 6. (Color online) Components of the ε_1 and ε_2 tensors obtained at the BSE level of theory. Solid, dashed, and dotted lines correspond to xx, yy, and zz components, respectively. We used a Lorentzian broadening of 0.1 eV.

obtained with the sc-hybrid functional (see Table V). This value is, however, smaller than those obtained at the DFT/PBE level of theory (10.31–10.40). Most of this difference is likely due to the difference between the PBE and G_0W_0 band gaps: The BSE calculations were performed starting from our G_0W_0 results, and the G_0W_0 gaps are larger than those obtained at PBE level.

Figure 6 displays the diagonal components of the computed ε tensors and shows that Ta_3N_5 is a strongly anisotropic material; the absorption onset strongly depends on the light polarization direction (we considered linearly polarized light in our BSE calculations). For polarization in the x direction the absorption edge occurs near 2.0 eV, while in the y and z directions the onsets of absorption are at 2.5 and 2.1 eV, respectively. Anisotropy among xx, yy, and zz components of ε_1 and ε_2 was also recently reported in Ref. [34] by Rashak, who found absorption edges of 2.2, 2.7, and 2.6 eV for x, y, and z directions, respectively, using full potential linear augmented-plane-wave (FPLAPW) method with the modified Becke-Johnson potential (mBJ).

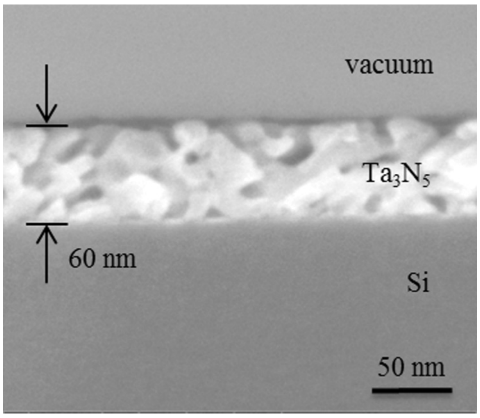

FIG. 7. Cross-sectional scanning electron micrograph of Ta_3N_5/Si showing a film thickness of 60 nm.

E. Spectroscopic ellipsometry

Figure 7 shows a cross-sectional SEM image of Ta_3N_5 on Si. The Ta_3N_5 layer forms as a porous network from an evaporated Ta film due to changes in density that occur in the film during the thermal oxidation and nitration steps [39]. According to XRD (Fig. 8), a crystalline Ta_3N_5 phase was produced with no indication of other tantalum nitride phases.

Our ellipsometry data can be described as a sum of oscillators derived from Drude and Tauc-Lorentz models. The Drude model describes light absorption arising from free carriers in metals and semiconductors [23]. In the case of Ta_3N_5, the n-type doping concentration is rather high due to reduced Ta species from N^{3-} anion vacancies, hence free carrier absorption is a valid assumption [30,45]. Free carrier absorption is generally visible at low energies down to the infrared [46] and below the band gap. The Drude model for intraband absorption is given by

$$\varepsilon = \varepsilon_\infty - \frac{A}{E^2 - i\Gamma E}, \tag{7}$$

where $A = \varepsilon_\infty E_p^2$, ε_∞ is the high frequency dielectric constant beyond the plasma energy E_p, Γ is a broadening parameter, and E is the photon energy [23].

The Tauc-Lorentz oscillator model for ε_2 with asymmetric peaks as products of the Tauc joint density of states and Lorentz

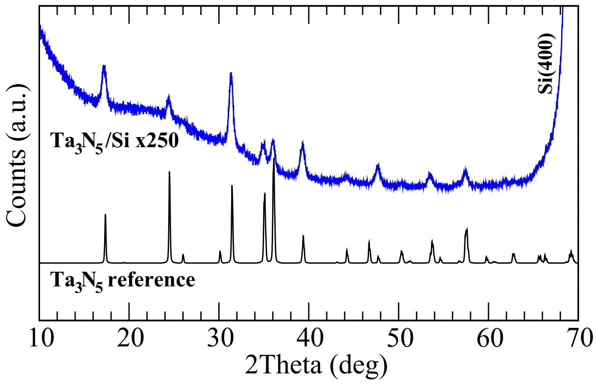

FIG. 8. (Color online) X-ray diffractogram of Ta_3N_5/Si prepared by oxidizing and nitriding 29 nm of Ta metal electron beam evaporated onto Si (Ta_3N_5 reference PDF 01-079-1533).

model (which only contains symmetric peaks for ε_2) is [47]

$$\varepsilon_2 = \begin{cases} \frac{AE_0\Gamma(E-Eg)^2}{\left(E^2-E_0^2\right)^2+\Gamma^2E^2}\frac{1}{E} & \text{when } E > E_g, \\ 0 & \text{when } E \leqslant E_g, \end{cases} \tag{8}$$

where A denotes optical transition matrix elements, E_0 is the peak transition energy, Γ is the peak broadening term, and E_g is the optical band gap. The ε_1 term is then calculated from ε_2 using Kramers-Kronig integration with the addition of another fitting parameter $\varepsilon_1(\infty)$ [47].

Since the Ta_3N_5 film is porous, the value of the dielectric function could be affected by the dielectric constant of air. To account for the void spaces in the Ta_3N_5 film, an effective medium approximation (EMA) model can be used with phases a and b denoting the Tauc-Lorentz/Drude models for Ta_3N_5 and void space, respectively. For our analysis, the Bruggeman approximation was used which assumes a spherical dielectric in a medium:

$$f_a\frac{\varepsilon_a-\varepsilon}{\varepsilon_a+2\varepsilon}+(1-f_a)\frac{\varepsilon_b-\varepsilon}{\varepsilon_b+2\varepsilon}=0, \tag{9}$$

where f_a and $(1-f_a)$ are the probabilities of finding ε_a and ε_b in a spherical space [48,49].

Drude, Tauc-Lorentz, and EMA models were applied to Ta_3N_5 grown on Si to determine the electronic structure of the nitride. Multiple Tauc-Lorentz oscillators were used to parametrize the various electronic transitions occurring in Ta_3N_5 [46]. Since the thickness of the film in question is known and held as a fixed parameter, direct numerical inversion (point-by-point fit) of the ellipsometry data was performed to first extract the dielectric function [46,50]. The optical model-derived dielectric function could then be compared to the direct inversion one. The mean square error (MSE) figure of merit was used to determine the quality of the model fit to the experimental Ψ and Δ values. A low MSE value indicates a good fit, hence it is desirable for MSE to approach a value of 1 [51]. Figure 9 shows ε_1 and ε_2 obtained by direct inversion of the experimental data and by the the Drude and Tauc-Lorentz models (with an EMA void fraction of 9.9 ± 4.5%). Table VI summarizes the fit parameter values for the oscillator curves shown in Fig. 9. The native SiO_2 thickness of 16.36 Å was fixed in this model to represent the SiO_2 layer between the Si substrate and the Ta_3N_5. While, in principle, the SiO_2 layer could grow thicker during Ta_3N_5 synthesis, we conducted a sensitivity analysis and found that the modeling results are robust with respect to changes in this parameter (see Fig. S2 in the Supplemental Material [38]). The Ta_3N_5 thickness of 60 nm was also fixed for parametrization. Our fitting parameters and experimental data agree well with previous Ta_3N_5 ellipsometry results [46].

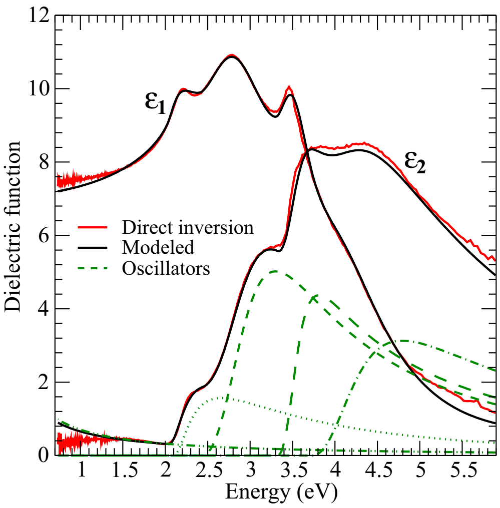

FIG. 9. (Color online) Directly inverted and modeled dielectric function of Ta_3N_5 including the Tauc-Lorentz, Drude, and EMA oscillator strengths used in the model. The estimated void fraction from the model is 9.9 ± 4.5%.

The E_g fit parameters that emerge from modeling the ellipsometry data describe the interband transitions occurring in Ta_3N_5. A unique model of this ellipsometry data required four E_g fit parameters at 2.1, 2.44, 3.32, and 3.74. The first transition occurs at $E_g = 2.1$ eV which agrees with the results obtained using *ab initio* calculations at the BSE/G_0W_0 level of theory (see Sec. III D) as well as previous experimental findings using UV-vis data [3,30,31]. This parameter was fixed because it is the first feature, correlates with the Tauc-Lorentz oscillator occurring at a peak transition energy of ~4 eV and agrees with previous literature findings [30,46]. Furthermore, the next transition occurring at $E_g = 2.44$ also agrees with the BSE/G_0W_0 optical spectra (shown in Figs. 4 and 5) and the absorption feature seen in Ref. [30] occurring at ~2.5 eV. A third interband transition occurs at an E_g of ~3.3 eV and agrees with the BSE/G_0W_0 optical spectra (Fig. 5) and with previous literature findings [46]. Finally, a fourth transition can be inferred from the parametrization that occurs at an E_g of 3.74 eV.

TABLE VI. Spectroscopic ellipsometry optical model parameters for Ta_3N_5 (see text).

A	Γ	E_0	E_g	$\varepsilon_1(\infty)$	EMA	MSE
Drude[a]						
0.78 ± 0.06	10 ± 2.6					
Tauc-Lorentz[b]						
136 ± 11	0.48 ± 0.01	2.0 ± 0.002	2.1	2.66 ± 0.1	9.9 ± 4.5	8.5
157 ± 18	1.18 ± 0.03	2.8 ± 0.02	2.44 ± 0.01			
399 ± 243	0.54 ± 0.07	3.46 ± 0.1	3.32 ± 0.04			
232 ± 64	1.32 ± 0.3	3.99 ± 0.09	3.74 ± 0.14			

[a] Defined as $\varepsilon = -A\Gamma/(E^2 + i\Gamma E)$ [24].

[b] Defined by Eq. (8).

Figure 5 shows good agreement for the real and imaginary parts of the dielectric function of Ta_3N_5 without voids obtained from parametrization of spectroscopic ellipsometry data and those computed by theory, where the three transitions occurring at 2.1, 2.44, and 3.32 eV are direct. We note that the dielectric function of Ta_3N_5 in Fig. 5 has higher values than the function in Fig. 9 because it is for the Ta_3N_5 layer only, without the addition of the void space EMA layer included in Fig. 9 for the porous Ta_3N_5 film.

IV. CONCLUSIONS

In summary, we presented a joint theoretical and experimental study of the optoelectronic properties of crystalline Ta_3N_5. Our optical spectra computed using the Bethe-Salpeter equation (BSE) within many-body perturbation theory are in excellent agreement with UV-vis [30] and ellipsometry measurements performed in this work. In particular, the optical gap (2.06 eV) computed from the G_0W_0 photoemission gap, taking into account spin-orbit coupling, exciton binding energy, and electron-phonon interaction, compares very well with the measured value of 2.1 eV. Both our calculations and ellipsometry measurements showed that the two previously poorly understood features present in the low energy part of the absorption spectrum originate from direct transitions between N and Ta states. We also found that Ta_3N_5 has an indirect gap about 0.2–0.3 eV lower than its smallest direct gap. For both direct and indirect gaps, results obtained at the G_0W_0 level of theory are in excellent agreement with those of recently proposed sc-hybrid functionals [14]. Theoretical BSE and experimental dielectric functions were found to be in good agreement.

Our theoretical results also showed that Ta_3N_5 is a highly anisotropic material with large electron and hole effective masses in certain directions (up to ∼3–3.5 electron masses), indicating that this material may have low mobilities, consistent with measured photocurrents in the literature that are well below the optical limit. In particular, we found that holes are in general heavier than electrons, consistent with the experimental finding [39] that the photocurrent scales primarily with the surface area of the films (large surface areas improve hole collection at the solid/liquid interface) rather than with thickness. These findings suggest that engineering the morphology of Ta_3N_5 films may help improve its photoelectrochemical performance.

ACKNOWLEDGMENTS

This work was supported by the National Science Foundation under the NSF Center CHE-1305124 for CCI Solar Fuels. This research used resources of the National Energy Research Scientific Computing Center, which is supported by the Office of Science of the U.S. Department of Energy under Contract No. DE-AC02-05CH11231. We thank Blaise Pinaud for providing experimental absorption data, and Yuan Ping, Dario Rocca, Marco Govoni, and Jonathan H. Skone for useful discussions.

---

[1] A. Fujishima and K. Honda, Nature (London) **238**, 37 (1972).

[2] S. Hu, M. R. Shaner, J. A. Beardslee, M. Lichterman, B. S. Brunschwig, and N. S. Lewis, Science **344**, 1005 (2014).

[3] W.-J. Chun, A. Ishikawa, H. Fujisawa, T. Takata, J. N. Kondo, M. Hara, M. Kawai, Y. Matsumoto, and K. Domen, J. Phys. Chem. B **107**, 1798 (2003).

[4] Z. Chen, T. F. Jaramillo, T. G. Deutsch, A. Kleiman-Shwarsctein, A. J. Forman, N. Gaillard, R. Garland, K. Takanabe, C. Heske, M. Sunkara, E. W. McFarland, K. Domen, E. L. Miller, J. A. Turner, and H. N. Dinh, J. Mater. Res. **25**, 3 (2010).

[5] Y. Li, T. Takata, D. Cha, K. Takanabe, T. Minegishi, J. Kubota, and K. Domen, Adv. Mater. **25**, 125 (2013).

[6] A. Ishikawa, T. Takata, J. N. Kondo, M. Hara, and K. Domen, J. Phys. Chem. B **108**, 11049 (2004).

[7] P. Hohenberg and W. Kohn, Phys. Rev. **136**, B864 (1964).

[8] G. Onida, L. Reining, and A. Rubio, Rev. Mod. Phys. **74**, 601 (2002).

[9] Y. Ping, D. Rocca, and G. Galli, Chem. Soc. Rev. **42**, 2437 (2013).

[10] E. E. Salpeter and H. A. Bethe, Phys. Rev. **84**, 1232 (1951).

[11] W. Kohn and L. J. Sham, Phys. Rev. **140**, A1133 (1965); J. P. Perdew and A. Zunger, Phys. Rev. B **23**, 5048 (1981).

[12] J. P. Perdew, K. Burke, and M. Ernzerhof, Phys. Rev. Lett. **77**, 3865 (1996).

[13] C. Adamo and V. Barone, J. Chem. Phys. **110**, 6158 (1999).

[14] J. H. Skone, M. Govoni, and G. Galli, Phys. Rev. B **89**, 195112 (2014).

[15] P. Giannozzi, S. Baroni, N. Bonini, M. Calandra, R. Car, C. Cavazzoni, D. Ceresoli, G. L. Chiarotti, M. Cococcioni, I. Dabo, A. Dal Corso, S. de Gironcoli, S. Fabris, G. Fratesi, R. Gebauer, U. Gerstmann, C. Gougoussis, A. Kokalj, M. Lazzeri, L. Martin-Samos, N. Marzari, F. Mauri, R. Mazzarello, S. Paolini, A. Pasquarello, L. Paulatto, C. Sbraccia, S. Scandolo, G. Sclauzero, A. P. Seitsonen, A. Smogunov, P. Umari, and R. M. Wentzcovitch, J. Phys.: Condens. Matter **21**, 395502 (2009).

[16] C. Hartwigsen, S. Goedecker, and J. Hutter, Phys. Rev. B **58**, 3641 (1998).

[17] R. Dovesi, R. Orlando, B. Civalleri, C. Roetti, V. R. Saunders, and C. M. Zicovich-Wilson, Z. Kristallogr. **220**, 571 (2005); R. Dovesi *et al.*, *CRYSTAL09 User's Manual* (University of Torino, Torino, 2009).

[18] T. Bredowa, M.-W. Lumey, R. Dronskowski, H. Schilling, J. Pickardt, and M. Lerch, Z. Anorg. Allg. Chem. **632**, 1157 (2006).

[19] P. J. Hay and R. W. Wadt, J. Chem. Phys. B **82**, 299 (1985); S. Piskunov, E. Heifets, R. I. Eglitis, and G. Borstel, Comput. Mater. Sci. **29**, 165 (2004).

[20] A. Marini, C. Hogan, M. Grning, and D. Varsano, Comput. Phys. Commun. **180**, 1392 (2009).

[21] M. Shishkin and G. Kresse, Phys. Rev. B **75**, 235102 (2007).

[22] D. Kammerlander, S. Botti, M. A. L. Marques, A. Marini, and C. Attaccalite, Phys. Rev. B **86**, 125203 (2012).

[23] H. Fujiwara, *Spectroscopic Ellipsometry: Principles and Applications* (John Wiley and Sons, Chichester, 2007).

[24] J. A. Woollam Co., I. Guide to Using WVASE32 (J. A. Woollam Co., Lincoln, 2010).

[25] N. E. Brese, M. O'Keeffe, P. Rauch, and F. J. DiSalvo, Acta Crystallogr. Sect. C **47**, 2291 (1991).

[26] E. Watanabe, H. Ushiyama, and K. Yamashita, Chem. Phys. Lett. **561–562**, 57 (2013).

[27] Y. Wu and G. Ceder, J. Phys. Chem. C **117**, 24710 (2013).

[28] J. Wang, W. Luo, J. Feng, L. Zhang, Z. Li, and Z. Zou, Phys. Chem. Chem. Phys. **15**, 16054 (2013).

[29] J. Wang, T. Fang, L. Zhang, J. Feng, Z. Li, and Z. Zou, J. Catal. **309**, 291 (2014).

[30] B. A. Pinaud, A. Vailionis, and T. F. Jaramillo, Chem. Mater. **26**, 1576 (2014).

[31] A. Dabirian and R. van de Krol, Appl. Phys. Lett. **102**, 033905 (2013).

[32] See Supplemental Material at http://link.aps.org/supplemental/10.1103/PhysRevB.90.155204 for a DOS plot with narrower broadening.

[33] C. M. Fang, E. Orhan, G. A. de Wijs, H. T. Hintzen, R. A. de Groot, R. Marchand, J.-Y. Saillard, and G. de With, J. Mater. Chem. **11**, 1248 (2001).

[34] A. H. Reshak, Comp. Mater. Sci. **89**, 45 (2014).

[35] J. Wang, J. Feng, L. Zhang, Z. Li, and Z. Zou, Phys. Chem. Chem. Phys. **16**, 15375 (2014).

[36] F. Tran and P. Blaha, Phys. Rev. Lett. **102**, 226401 (2009); A. D. Becke and E. R. Johnson, J. Chem. Phys. **124**, 221101 (2006).

[37] M. Rérat, R. Orlando, and R. Dovesi, J. Phys.: Conf. Ser. **117**, 012016 (2008); B. G. Johnson and M. J. Frisch, Chem. Phys. Lett. **216**, 133 (1993).

[38] See Supplemental Material at http://link.aps.org/supplemental/10.1103/PhysRevB.90.155204 for further comparison of lattice parameters and band gaps obtained with and without semicore states in the valence partition.

[39] B. A. Pinaud, P. C. K. Vesborg, and T. F. Jaramillo, J. Phys. Chem. C **116**, 15918 (2012).

[40] Y. Ping, D. Rocca, and G. Galli, Phys. Rev. B **87**, 165203 (2013).

[41] G. D. Mahan, *Many-Particle Physics* (Kluwer Academic/Plenum, New York, 2000), p. 433.

[42] M. A. Smondyrev, Theor. Math. Phys. **68**, 653 (1986).

[43] S. Baroni, S. de Gironcoli, A. Dal Corso, and P. Giannozzi, Rev. Mod. Phys. **73**, 515 (2001).

[44] M. Fox, *Optical Properties of Solids* (Oxford University Press, New York, 2001), p. 78.

[45] S. S. K. Ma, T. Hisatomi, K. Maeda, Y. Moriya, and K. Domen, J. Am. Chem. Soc. **134**, 19993 (2012).

[46] E. Langereis, S. B. S. Heil, H. C. M. Knoops, W. Keuning, M. C. M. van de Sanden, and W. M. M. Kessels, J. Phys. D: Appl. Phys. **42**, 073001 (2009).

[47] G. E. Jellison and F. A. Modine, Appl. Phys. Lett. **69**, 371 (1996).

[48] D. A. G. Bruggeman, Ann. Phys. **416**, 636 (1935).

[49] G. A. Niklasson, C. G. Granqvist, and O. Hunderi, Appl. Optics **20**, 26 (1981).

[50] H. Fujiwara and M. Kondo, Phys. Rev. B **71**, 075109 (2005).

[51] C. M. Herzinger, P. G. Snyder, F. G. Celii, Y. C. Kao, D. Chow, B. Johs, and J. A. Woollam, J. Appl. Phys. **79**, 2663 (1996).